Nitrogen-Doped Graphene-Rich Catalysts Derived from Heteroatom Polymers for Oxygen Reduction in Nonaqueous Lithium–O_2 Battery Cathodes

Gang Wu,[†,*] Nathan H. Mack,[‡] Wei Gao,[†] Shuguo Ma,[§] Ruiqin Zhong,[†] Jiantao Han,[†] Jon K. Baldwin,[†] and Piotr Zelenay[†]

[†]Materials Physics and Applications Division and [‡]Division of Chemistry, Los Alamos National Laboratory, Los Alamos, New Mexico 87545, United States and [§]Department of Chemical Engineering, University of South Carolina, Columbia, South Carolina 29208, United States

ABSTRACT In this work, we present a synthesis approach for nitrogen-doped graphene-sheet-like nanostructures *via* the graphitization of a heteroatom polymer, in particular, polyaniline, under the catalysis of a cobalt species using multiwalled carbon nanotubes (MWNTs) as a supporting template. The graphene-rich composite catalysts (Co-N-MWNTs) exhibit substantially improved activity for oxygen reduction in nonaqueous lithium-ion electrolyte as compared to those of currently used carbon blacks and Pt/carbon catalysts, evidenced by both rotating disk electrode and Li–O_2 battery experiments. The synthesis–structure–activity correlations for the graphene nanostructures were explored by tuning their synthetic chemistry (support, nitrogen precursor, heating temperature, and transition metal type and content) to investigate how the resulting morphology and nitrogen-doping functionalities (*e.g.*, pyridinic, pyrrolic, and quaternary) influence the catalyst activity. In particular, an optimal temperature for heat treatment during synthesis is critical to creating a high-surface-area catalyst with favorable nitrogen doping. The sole Co phase, Co_9S_8, was present in the catalyst but plays a negligible role in ORR. Nevertheless, the addition of Co species in the synthesis is indispensable for achieving high activity, due to its effects on the final catalyst morphology and structure, including surface area, nitrogen doping, and graphene formation. This new route for the preparation of a nitrogen-doped graphene nanocomposite with carbon nanotube offers synthetic control of morphology and nitrogen functionality and shows promise for applications in nonaqueous oxygen reduction electrocatalysis for Li–O_2 battery cathodes.

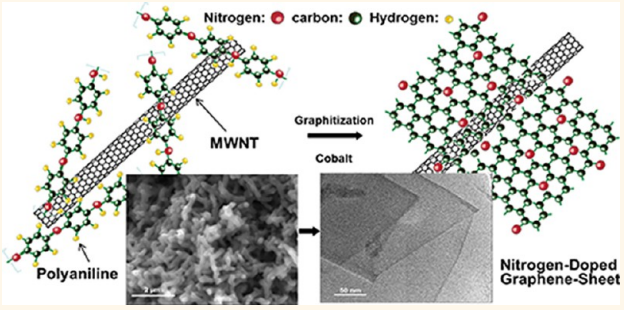

KEYWORDS: graphene · nitrogen doping · heteroatom polymer · non-precious-metal catalysts · oxygen reduction · Li–O_2 battery

The oxygen reduction reaction (ORR) is an important electrochemical reaction, underlined by the strong research interests in a variety of electrochemical energy storage and conversion technologies such as low-temperature fuel cells and metal–air batteries.[1] A high ORR overpotential has been the main obstacle to making these technologies viable, and therefore, major efforts have been devoted to discovering cost-effective and efficient ORR catalysts in traditional aqueous media.[2–5] Recently, -ORR in nonaqueous lithium-ion electrolyte has become a key reaction in Li–O_2 (air) battery cathodes and received considerable attention. As potential next-generation energy storage devices, the Li–O_2 batteries abandon the intercalation electrodes in traditional Li-ion batteries, and the Li ions react directly with O_2 from the air in a porous electrode. As a result, the unique battery chemistry and electrode architecture provide a greatly increased specific energy density (theoretical value of 5200 Whkg^{-1}),[6] holding promise to meet the energy density targets set for batteries in automotive applications (1700 Whkg^{-1}, a value comparable to the usable energy content of gasoline).[7,8]

A Li–O_2 cell is a battery/fuel cell hybrid,[9,10] with the cathode similar to an oxygen

* Address correspondence to wugang@lanl.gov.

Received for review July 20, 2012 and accepted October 4, 2012.

Published online October 04, 2012
10.1021/nn303275d

cathode in a fuel cell, but with H_2 oxidation at the anode being replaced with oxidation of metallic Li. The use of nonaqueous electrolytes in a Li−O_2 battery has the advantage of alleviating the parasitic corrosion of Li metal at the anode, which occurs in aqueous media.[8,11] A major distinction of ORR between aqueous and nonaqueous media is that the preferred reduction products in aqueous electrolyte are H_2O or H_2O_2, while insoluble lithium−oxygen species (Li_2O or Li_2O_2) form in nonaqueous electrolytes, readily leading to passivating layers on the cathode catalyst surface. The catalysis mechanisms for ORR and approaches for efficient catalysts are certainly different for nonaqueous Li^+ electrolytes, relative to their aqueous counterparts. Thus, development of active cathode catalysts compatible with the nonaqueous Li^+−O_2 systems remains a significant challenge in Li−O_2 battery technologies.

At present, a large ORR overpotential is observed on carbon cathode catalysts (Vulcan XC-72, Ketjenblack, BlackPearl, *etc.*) in the nonaqueous Li^+−O_2 systems, causing the battery discharge voltage to be considerably reduced (2.5 V) and the overall charge−discharge cyclic energy efficiency to be low.[12] In principle, the ORR overpotential can be reduced by accelerating the kinetic reaction with the development of advanced catalysts.[13−15] For example, nanostructured α-MnO_2 nanowires have been found to be more ORR active than carbon black catalysts.[14] However, their low overall electron conductivity and insufficient activity still result in commensurately low energy efficiency. Bifunctional precious-metal-based PtAu/C catalysts exhibit improved oxygen reduction and evolution activity in the Li^+−O_2 systems.[16] Unfortunately, the use of precious metals in cathode catalysts makes them prohibitively expensive and limits their widespread implementation in Li−O_2 batteries. Thus, the battery technologies are in dire need of an efficient and cost-effective alternative to Pt-based catalysts for their nonaqueous electrolyte-based ORR cathodes.[17]

Advances in nanostructured catalyst design and synthesis are necessary to fully harvest the high-energy densities offered by this battery technology.[18,19] Recently, stand-alone graphene and graphene oxide (GO) have been explored as *ex situ* supports in the ORR catalysts.[20−24] For example, nitrogen-doped graphene materials were prepared by annealing GO with different nitrogen precursors.[25] However, the graphene materials produced directly from the reduction of GO are not part of the active catalysts and only act as *ex situ* supports. In a similar manner, nitrogen-doped graphene nanosheets (GNSs) synthesized from GO through heat treatment with high-purity ammonia once were examined in Li−O_2 batteries.[26] Although a higher discharge capacity of 8705 $mAhg^{-1}$ was measured with the GNSs cathode, the battery discharge voltage plateau observed in the electrode only reaches 2.58 V, illustrating that the very high ORR overpotential still exists.[26]

In contrast, this work uses nitrogen-doped graphene-rich composite catalysts that have been developed from a graphitization process of a heteroatom polymer (polyaniline, PANI) under the catalysis of a cobalt species, using multiwalled carbon nanotubes (MWNTs) as a supporting template. Compared to the reported metal-free graphene catalysts,[25,26] the addition of the Co species significantly improves the catalytic activity for ORR. Although the resulting Co_9S_8 in the catalyst plays a negligible role in ORR, Co species are found to be indispensable during the catalyst synthesis to achieve high activity, due to its effects on the resulting catalyst morphology and structure. In particular, pyrrolic N is usually the dominant species when using ammonia as a dopant;[26] however, this work finds a high level of quaternary and pyridinic N when the graphene composite catalysts are synthesized in the presence of Co, a finding that is concomitant with much improved activity for ORR. We believe the unique properties of the MWNTs acting as a support are partially responsible for these improvements. Beneficial mass and electron transport, specific interactions between active site and CNTs, as well as high corrosion resistance[27,28] can all improve cathode performance when using MWNTs to template the polymer graphitization process. In addition, promotional roles were found for MWNTs during the formation of the graphene composites, showing extended multilayered graphene sheet morphologies rather than the agglomerated bubble-like graphene structures observed in the ketjenblack (KJ)-templated materials. Importantly, unlike the traditional synthetic approaches for graphene materials,[29,30] the *in situ* formation of nitrogen-doped graphene sheets directly from heteroatom polymers provides a new route for preparation of graphene nanocomposites, offering controlled morphology and nitrogen functionality with enhanced oxygen reduction catalytic activity.

RESULTS AND DISCUSSION

Synthesis of Nitrogen-Doped Graphene Composites. A synthesis scheme for nitrogen-doped graphene-rich composites is shown in Figure 1. As a both nitrogen and carbon source, the heteroatom polymer, PANI, was graphitized at elevated temperature with the catalysis of a Co species. Due to their structural similarities, the aromatic in PANI may facilitate the graphitization process and form nitrogen-doped graphene-sheet-like structures. MWNTs proved to be an effective supporting template for the formation of graphene, as compared to traditional carbon black supports. As the MWNTs still obviously present in the catalysts after heating treatment, the graphene-like sheets are likely not derived from the carbon nanotubes. Optimized

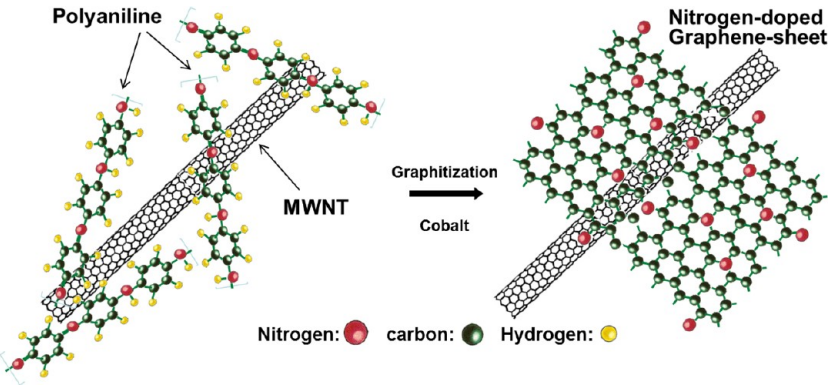

Figure 1. Scheme of the formation for nitrogen-doped graphene sheets derived from polyaniline and Co precursors using MWNTs as a template.

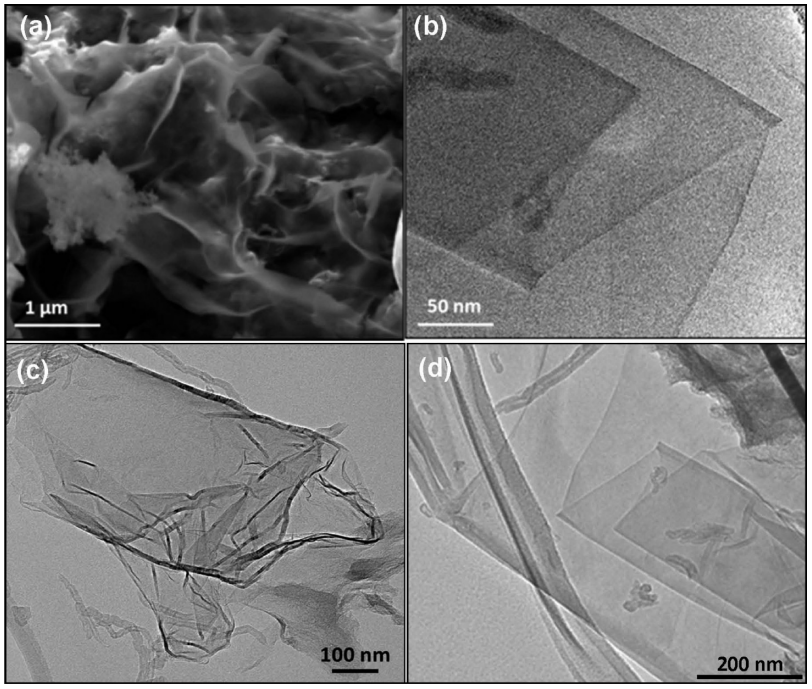

Figure 2. SEM (a) and HR-TEM (b–d) images of the graphene-rich nanocomposites observed in Co-N-MWNT catalysts.

heating temperatures lead to a maximum in the yield of graphene structures in the final catalyst. Properly selecting the transition metal and metal content in synthesis is key to controlling the graphene morphology and doped nitrogen structure. In this work, we will describe this newly developed route toward the controllable synthesis of nitrogen-doped graphene composite catalysts for ORR in nonaqueous Li–O_2 battery cathodes.

Morphology and Structure. Electron microscopy images of the prepared nanocomposite catalysts are shown in Figure 2. It can be seen that the graphene-sheet-like structures are dominant, which wrap around the MWNTs. The large and extended sheets with lateral dimensions in the hundreds of nanometers turn out to be wrinkled on the edges and are most likely due to nitrogen doping. They appear to be relatively thin according to TEM imaging, but the exact thickness is yet to be determined from higher-resolution TEM or Raman spectroscopy. Compared to traditional approaches to single- and few-layer graphene structures,[29,30] this synthesis of doped graphene materials *via* a graphitization process is a new and more cost-effective route. Recently, nitrogen-doped graphene materials were also reported and derived from the reduced GO (RGO) followed by additional treatment or chemical reaction to achieve the nitrogen doping.[25,26] However, there is a delicate difference between the RGO and graphene. In this work, however, the graphitization approach is completely different from the RGO protocol. Since we believe that our graphene-like structure is also highly doped and defected, the detailed comparison of RGO-derived graphene and our PANI/Co-derived graphene in structures is still under investigation.

The resulting graphene-rich catalyst exhibited much improved ORR activity in nonaqueous electrolyte and

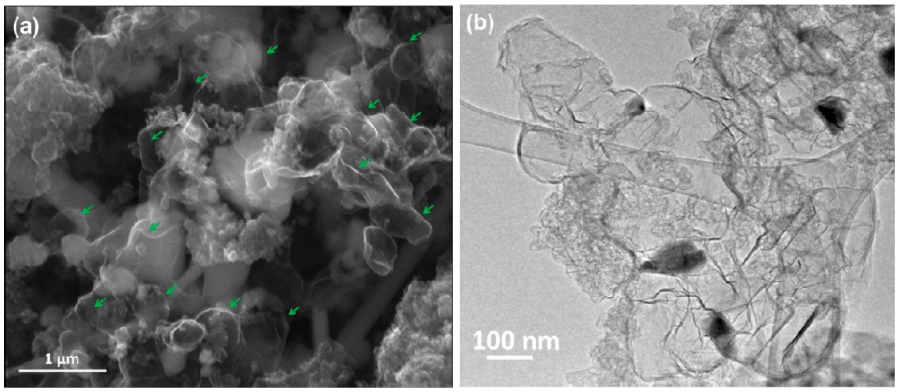

Figure 3. Morphology of Co-N-KJ-based catalyst with agglomerated graphene-sheet-like structures (marked by green arrows): (a) SEM and (b) TEM images.

cathode performance in a Li–O_2 battery cell, relative to currently used carbon and Pt-based catalysts. The synthesis–structure–activity correlations for the nanocomposite were systematically explored in terms of their morphology and structure as functions of synthetic chemistry including supporting materials, nitrogen precursors, heat-treatment temperatures, and transition metal types and content.

MWNTs as a Template. The morphology of the synthesized graphene sheet structures was found to greatly depend on the supporting template used during catalyst synthesis. Unlike a substantial fraction of the extended multilayered graphene sheets observed in the MWNT-supported catalyst (Co-N-MWNTs), the KJ-supported Co-N-KJ catalyst is dominated by agglomerated bubble-like graphene structures (Figure 3). This lower level of agglomeration is likely due to the unique surface properties and morphologies of the MWNTs. Consistent with the observed catalyst morphology, MWNT supports provide a higher surface area and abundant mesopores in the Co-N-MWNTs catalyst (278 $m^2\ g^{-1}$), relative to the KJ-supported catalysts (101 $m^2\ g^{-1}$) (Figure S1 in Supporting Information).

When O_2 is electroreduced in nonaqueous Li-ion electrolytes, insoluble lithium–oxygen compounds (Li_2O_2 or Li_2O) are formed and cover the catalyst surface, blocking the active catalytic sites and O_2 diffusion channels and ultimately resulting in catalyst performance degradation. Relative to the KJ-supported catalyst, an improved tolerance to these insoluble lithium–oxygen compounds was observed with the Co-N-MWNT catalysts. Figure S2 shows the steady-state oxygen reduction polarization plots continuously recorded up to nine cycles without charging. The Co-N-MWNT catalyst retains 65% of its activity at 2.0 V, as compared to only 10% retention for the Co-N-KJ catalyst. This performance enhancement is possibly due to the higher surface area and more abundant mesopores in the MWNT-based catalysts, both leading to a higher density of active sites and improved mass transport properties within Co-N-MWNT cathodes.

Roles of Cobalt and Aromatic Polymers. As shown in HR-TEM images (Figure 4), both PANI-derived Co-free (N-MWNTs) and ethylenediamine (EDA)-derived Co-based catalysts do not contain such graphene-sheet-like structures and have relatively poorer ORR catalytic activity (Figure S3). Specifically, in the absence of Co, only amorphous carbon was formed from the PANI graphitization at high temperatures (900 °C), suggesting that the Co species is required to form highly graphitized carbon nanostructures.

In addition, catalyst nanostructures are directly related to the carbon–nitrogen precursors used during synthesis. Unlike the PANI-Co-derived samples, the morphology of the EDA-Co sample is dominated by different carbon nanostructures, including nanotubes and onion-like carbon, resulting from the carbonization of interlinked $[\text{-Co(EDA)}_4\text{-}]_n$ complexes.[31] The significant differences in the carbon morphology observed in these catalysts along with their varied ORR activity imply that the type of the graphitized carbon nanostructures in the catalysts is critical to catalytic activity for the ORR in the nonaqueous electrolytes. In particular, the aromatic structures in PANI and their close resemblance to graphene are likely key to forming graphene-sheet-like structures with improved catalytic activity.

Heat Treatment. The morphology of the graphene-rich Co-N-MWNT catalysts is dependent on the temperature used during synthesis. XRD and BET analyses were used to study crystalline phases and the surface area of the Co-N-MWNT catalysts, respectively, as a function of heating temperatures ranging from 600 to 1000 °C. Before the heat treatment, the well-resolved crystalline structures observed are assignable primarily to the excess oxidant $(NH_4)_2S_2O_8$ along with a small amount of PANI. Following heat treatment, only diffraction peaks associated with Co_9S_8 (2θ = 15.3, 29.7, 31.2, 39.4, 47.5, and 51.9°)[32,33] are observed from 600 to 1000 °C (Figure S4a), with all PANI signals being completely removed. The sulfur originates from the $(NH_4)_2S_2O_8$ initially used as the oxidant in the aniline polymerization process. BET surface area analysis of

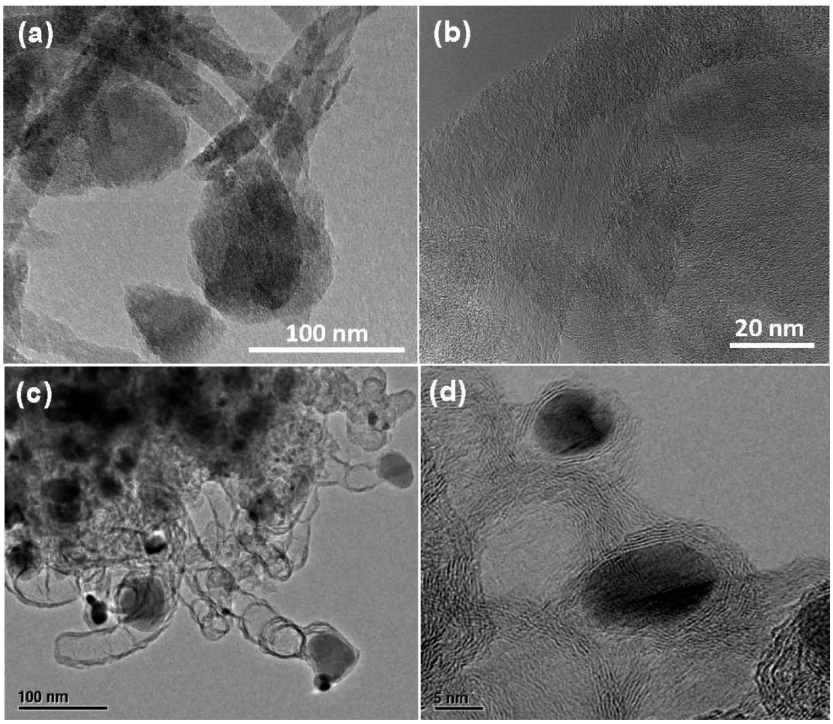

Figure 4. HR-TEM images of (a,b) metal-free N-MWNTs and (c,d) ethylenediamine (EDA)-derived Co catalysts.

these samples indicates that the heat treatment during synthesis is crucial to forming a high-surface-area catalyst (Figure S4b). Prior to heat treatment, the deposition of *in situ* polymerized aniline fills the pores of the MWNT support (~230 $m^2\ g^{-1}$), and the resulting material has a significantly reduced surface area (~5 $m^2\ g^{-1}$). High BET surface areas are not observed until the heating temperatures are increased beyond 800 °C (177 $m^2\ g^{-1}$), with a maximum at 900 °C (278 $m^2\ g^{-1}$). This process also results in the morphology of the PANI nanofibers changing to spherical particles as the postheating temperature increases up to 800 °C. The graphene-sheet-like structures grown over the solid particles are only observed when the heat-treatment temperature reaches 900 °C (Figure S5). The observed graphene-sheet-like structures are in good agreement with the highest BET surface areas and maximum catalyst activity measured with the samples synthesized at 900 °C, due to the higher surface area of graphene materials compared to other types of carbon materials.[34]

XPS was used to correlate the elemental content and doped nitrogen functionality of the Co-N-MWNT catalysts with their measured ORR activity. Elemental compositions for C and N in Co-N-MWNT catalysts as a function of heat treatment are measured by relative XPS signal intensities (Figure S6). The C 1s XPS spectra of the catalysts indicate that raising the temperature leads to an increase in the content of low-binding-energy carbon, presumably due to the formation of graphitic carbon at the catalyst surface. The increase in carbon content is accompanied by a decline in nitrogen content. It is of note, however, that the decreased nitrogen content with the temperature does not lead to a commensurate drop in ORR activity. This may suggest that the ORR activity is not dependent on the total amount of incorporated nitrogen but more on how the nitrogen is incorporated into doped nitrogen–carbon hybrid nanostructures. Nitrogen functionality determined by N 1s XPS spectra reveals subtle differences in the nitrogen doping of the carbon structures controlled by the heating temperatures during synthesis (Figure 5). These spectra can generally be fitted with two primary peaks, which correspond to pyridinic N (398.6 ± 0.3 eV) and pyrrolic N (400.3 ± 0.3 eV)/quaternary N (401.3 ± 0.3 eV), respectively.[35−37] Pyridinic N consists of nitrogen atoms doped at the edges of a graphitic carbon layer. "Graphitic" nitrogen atoms are labeled as quaternary N that is within a graphite plane and bonded to three carbon atoms. In addition, the quaternary N may include protonated pyridine species remaining in the catalysts.[35,38] Primarily, nitrogen can be viewed as an n-type carbon dopant that assists in the formation of disordered carbon nanostructures and donates electrons into the graphene domain, theoretically facilitating the ORR.[3] This series of spectra illustrate that the low-binding-energy pyridinic peak found at 398.6 eV starts forming at a low temperature (600 °C), resulting from nitrogen doped at the edge of a graphitized carbon plane, as opposed to the secondary (R-N-R) and tertiary (R-N═R) amines found in the PANI starting materials.[38,39] In the meantime, pyrrolic N also found at lower temperatures (600–700 °C) is associated with nitrogen atoms that

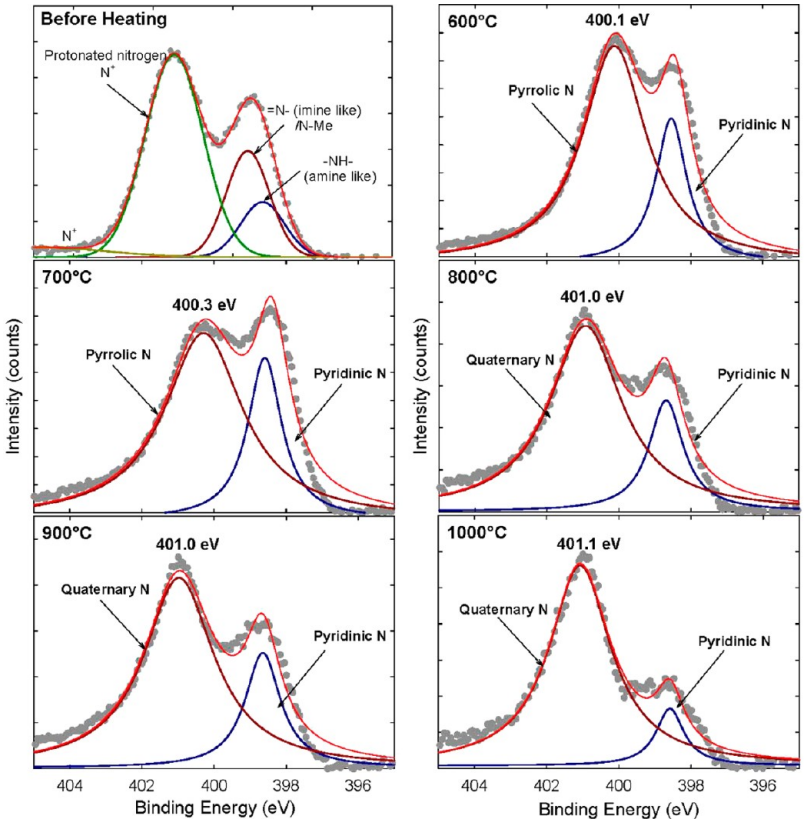

Figure 5. XPS N 1s spectra of Co-N-MWNT catalysts as a function of heating treatment temperature.

are incompletely incorporated into the carbon lattice. Yet, as the heat-treatment temperature increases, the high-binding-energy peak gradually shifts to higher energies (from 400.1 to 401.1 eV), indicating a conversion from pyrrolic to quaternary N. Thus, the pyrrolic nitrogen atom in the incomplete five-sided ring is thermally unstable and transforms into a quaternary nitrogen atom inside the graphitic carbon plane when the heating temperature is above 800 °C. It is worth noting that extremely high temperatures (1000 °C) result in a significant reduction in pyridinic N on the prepared catalyst and is accompanied with a commensurate drop in ORR activity.

Transition Metal Type and Content. The morphology, structure, and activity of catalysts derived from PANI are controllable by selecting the type of transition metal (Co *vs* Fe) used during synthesis (Figure S7).[40] Graphene-sheet-like structures abundantly exist in the Co-based catalyst but not in the Fe-based one. The relative content of pyridinic N in Co-based catalysts is obviously higher than that observed with the Fe-based catalysts. Importantly, X-ray absorption spectroscopy indicates the metallic Co–Co shell is the main species in the Co catalysts, while the Fe–N_x coordination is the dominant structure in the Fe catalysts. During catalyst synthesis, Co species may promote nitrogen doping into graphene, forming abundant CN_x structures as potential active sites for the ORR. On the other hand, even at high pyrolysis temperatures, Fe can be stabilized by a nitrogen–carbon network in the form of pyrrolic and/or pyridinic species and seems to participate directly in the active ORR sites.[40,41] Although the Fe-based catalysts usually exhibit higher activity for ORR in aqueous electrolyte,[2] in this work, the Co-based catalysts show superior performance in the nonaqueous media (Figure S8). Thus, these results suggest that the optimal active site structures for the ORR in nonaqueous media are likely not the same as in traditional aqueous systems.

The graphene-rich catalyst morphology and structures were further studied as a function of Co content during Co-N-MWNTs catalyst synthesis ranging from 0 to 30 wt %. XRD analysis indicates that the Co_9S_8 phase is only observed when Co content is above 5 wt % (Figure S9a). The BET surface areas of these catalysts were also determined as a function of the Co content, increasing from 65 $m^2\ g^{-1}$ for Co-free samples to 100 $m^2\ g^{-1}$ for samples with 5 wt % Co and to 278 $m^2\ g^{-1}$ for 30 wt % Co-derived catalysts (Figure S9b). Correlation of catalyst morphology (SEM images in Figure S10) and the Co content indicates that the Co-free sample is highly uniform with many interconnected carbon structures, and an increase in the Co content leads to a more heterogeneous catalyst. When the Co content increases above 5 wt %, graphene-like structures are observed, accompanied with the simultaneous formation of the Co_9S_8 phase. Thus, the presence of Co species during the heating treatment step

is indispensable to the *in situ* formation of graphene. In turn, the formation of high-surface-area graphene sheets in catalysts obtained at high Co content may be directly associated with the increase of BET surface area, corresponding the maximum ORR activity.

The nitrogen-doping functionalities in Co-N-MWNT catalysts were also studied as a function of Co content used in synthesis. XPS analysis shows that an initial increase of the Co content up to 2.5 wt % leads to a rise in the total nitrogen in the final catalysts (Figure 6). However, when higher Co content was used, a gradual decline in the nitrogen is observed in the resulting catalysts, until a plateau is reached at a Co content of 10 wt %. The N 1s spectra also show two major peaks associated with pyridinic and quaternary nitrogen species. Importantly, the pyridinic-to-quaternary N ratio increases from 0.58 for Co-free samples to 0.79 for the catalysts synthesized from Co content exceeding 10 wt %. The observed plateau of pyridinic-to-quaternary N ratio correlates well with the increasing ORR activity, suggesting that pyridinic nitrogen atoms doped at the edge of carbon structures may be critical to the ORR performance enhancement in the nonaqueous electrolyte. The Co species seem to facilitate the formation of such active nitrogen functionalities.

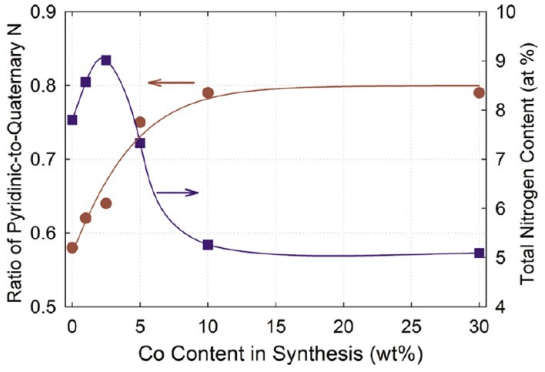

Figure 6. Dependence of doped nitrogen type and content on Co content used in synthesis.

Raman analysis for the graphene-rich Co-N-MWNT catalyst as a function of Co content is shown in Figure 7. Each spectrum was fitted to a series of four Lorentzian peaks, centered at 1200, 1350, 1510, and 1590 cm^{-1}. These spectra are dominated by characteristic carbon resonances around 1590 cm^{-1} (G band) and 1350 cm^{-1} (D band), which correspond to the planar motion of sp^2-hybridized carbon atoms in an ideal graphene layer and the defects in graphene structure including the carbon atoms close to the edge of a graphene sheet, respectively.[42] Consequently, the ratio of these peaks gives an indication of the overall crystallinity associated with the carbon structures. Additionally, two broad signals at *ca.* 1200 and 1510 cm^{-1} are also convolved in the overall Raman spectrum. They are associated with carbon atoms outside of a perfectly planar graphene network (such as aliphatic or amorphous structures) and integrated five-membered rings or heteroatoms in graphene sheet structures,[42,43] respectively.

While the Co-free PANI-MWNT and Co-N-MWNT (2.5 wt % Co) samples show nearly identical Raman spectra, pronounced differences are observed when the Co content is increased to 5 wt %. This observation is in good agreement with the formation of graphene at a Co content of 5 wt %. G and D peaks become manifested in the 30 wt % Co sample that is dominated by graphene-like structures (Figure 1 and Figure S10). The decreased peak intensities at 1200 and 1510 cm^{-1} with Co content suggest that the carbon matrix contains a

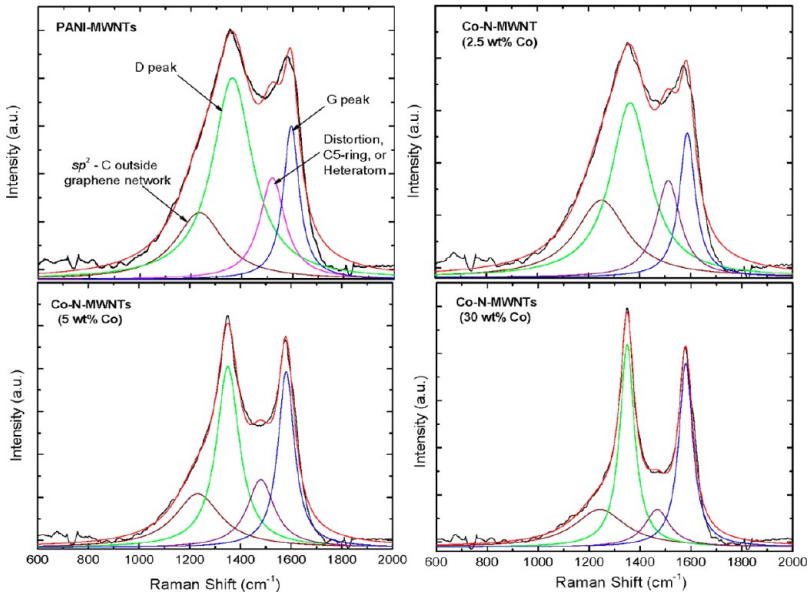

Figure 7. Raman spectra of Co-N-MWNT catalysts synthesized from different Co contents (black lines are experimental data; the red lines are fitted results).

lower ratio of amorphous carbon or distorted structures such as integrated heteroatoms within the graphene planes. This is consistent with the results of the XPS analysis discussed above, which indicates less nitrogen doping at higher Co-content-derived catalysts. The simultaneous occurrence of features in the Raman spectra suggest that "ordered" graphitized carbon (most likely graphene-sheet-like structures) can be derived from the aromatic polymer (PANI) decomposition only in the presence of high Co content. Co species here are not only helping the formation of catalytic sites but also catalyzing the formation of graphitized carbon.

Oxygen Reduction Activity in Rotating Disk Electrode (RDE) Tests. The ORR activity of the Co-based nitrogen-doped graphene composite catalysts in 0.1 M $LiPF_6$ 1,2-dimethoxyethane (DME)[12] was studied using a RDE and compared with that of other cathode catalysts (KJ, metal-free N−C(KJ), and Pt/C) (Figure 8a). As for the shape of the measured polarization plots, unlike in the aqueous electrolyte, no saturated plateau at low potential range is achieved for ORR in the nonaqueous Li^+-O_2 electrolyte.[44] Instead, a broad peak was observed at the low potential range. This is due to the formation of insoluble lithium−oxygen compounds that cover the catalyst surface, ultimately resulting in a degradation of catalyst activity. In the case of the thermally treated metal-free N−C sample, the introduction of nitrogen leads to an obvious improvement in the ORR activity in the kinetic region, relative to the nitrogen-free KJ carbon sample. However, the metal-free N−C materials appear unable to effectively reduce O_2 yet. A substantial improvement in the ORR activity was only achieved with an addition of Co. The resulting Co-based catalysts exhibit superior performance compared to Pt catalysts, reflected by a positive difference in the ORR half-wave potential, $E_{1/2}$ (2.42 V for Pt *vs* 2.77 V for Co-N-MWNTs) and, to a lesser degree, by a difference in the onset potential (3.0 V for Pt *vs* 3.1 V for Co-N-MWNTs). The low overpotential measured with the Co-based catalysts indicates that more intrinsically active sites are formed under the catalysis of the Co species. While a similar ORR kinetic activity was obtained with both KJ- and MWNT-supported Co-based catalysts, the MWNT support delivered much improved performance in the mass transfer potential region, due to high surface area and the facilitated graphene morphology, as well as the dominant mesopore in resulting catalysts as discussed above (Figure S1).

The roles of different components existing in the Co-N-MWNT composite catalyst can be convolved and difficult to isolate. To test each component separately, Co_9S_8 synthesized with a hydrothermal method,[32] stand-alone RGO,[45] and MWNT supports were studied as separate catalysts in nonaqueous Li^+ electrolytes for the ORR (Figure 8b). Their activity was compared with

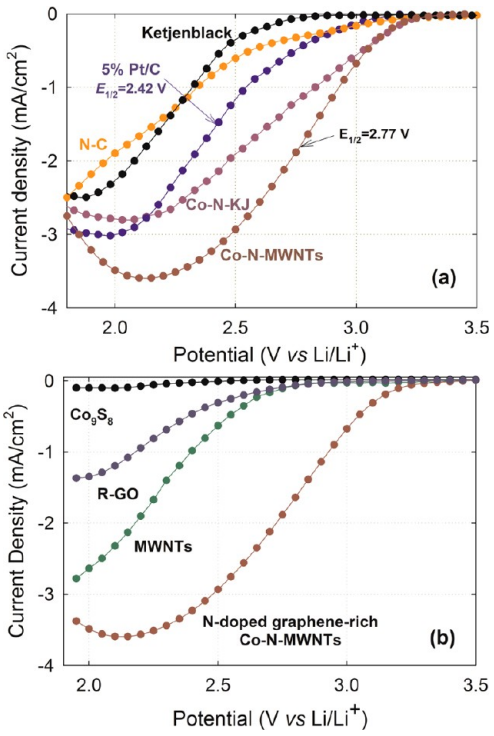

Figure 8. RDE testing results for the ORR at 25 °C in oxygen-saturated 0.1 M $LiPF_6$ in 1,2-dimethoxyethane electrolyte at a rotating speed of 900 rpm on (a) various catalyst samples and controls and (b) different components found in the best performing Co-N-MWNT composite catalysts.

the Co-N-MWNT catalysts containing nitrogen-doped graphene-rich structures. The Co_9S_8 shows insignificant ORR activity in the nonaqueous electrolyte. In addition, both RGO and MWNT samples present much lower performance as compared to the Co-N-MWNT catalysts in terms of their onset and $E_{1/2}$ potentials. This comparison suggests that the *in situ* formed N-doped graphene structures are mainly responsible for the high activity measured with the Co-N-MWNT catalysts. In addition, 1.0 M HNO_3 was used to leach out the Co_9S_8 species from the Co-N-MWNT catalysts, and the resulting sample still exhibits comparable ORR activity to the unleached catalyst (Figure S11). This direct assessment indicated that the Co_9S_8 species play a minor role in the Co-N-MWNT catalysts for ORR in nonaqueous Li^+-O_2 systems.

The exact structure of the active site(s) created during the thermal treatment of carbon, nitrogen, and metal precursors remains the subject of an intense debate in the field.[19] Nevertheless, the catalytic sites are thought to form during the thermal treatment step, and thus the overall catalytic activity is expected to be strongly dependent on the heating temperature. This temperature effect was investigated by measuring the ORR activity of the Co-N-MWNT catalysts synthesized at temperatures ranging from 600 to 1000 °C (Figure 9a). The ORR activity determined by onset potential and $E_{1/2}$ increases with heating temperature, with a

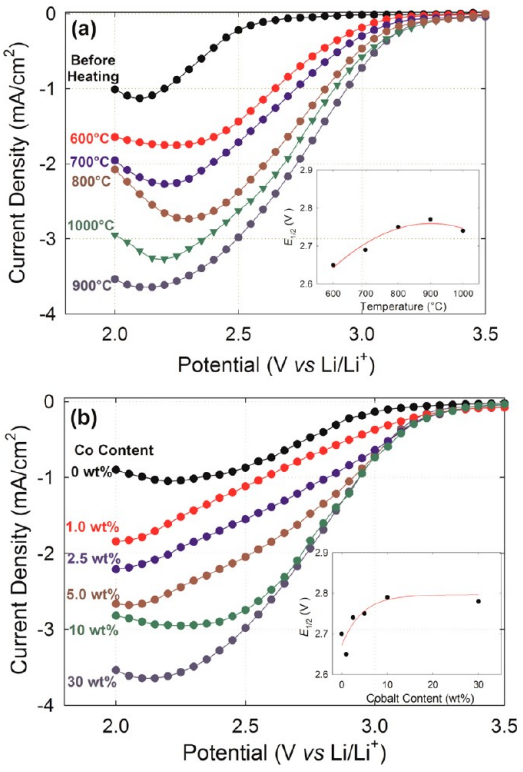

Figure 9. ORR activity of Co-N-MWNT catalysts as functions of the heating treatment temperature (a) and Co content (b) in synthesis; insets are correlations of heat-treatment temperature (a) and cobalt content (b) with resulting catalyst activity ($E_{1/2}$).

maximum at 900 °C, followed by a slight drop at a higher temperature (1000 °C). This behavior is likely related to the highest surface area and the most optimal nitrogen-doping structures (ratio of pyridinic to quaternary N) that result from the heating treatment at 900 °C. The activity decrease at elevated temperatures (1000 °C) may be due to the reduction of surface area caused by the possible collapse of the carbon structures[46] or the reduction in pyridinic N content (Figure 5). As one of the major components in the catalysts, Co_9S_8 species become more agglomerated at higher temperatures (Figure S12). However, as Co_9S_8 exhibits insignificant ORR activity in the nonaqueous Li^+-O_2 system, morphology change of Co_9S_8 is not expected to influence the ORR activity.

The Co species are necessary for the creation of highly active ORR catalysts; therefore, catalytic activity was also studied as a function of the Co content from 0 to 30 wt % in the initial mixture of precursors (Figure 9b). The activity in the kinetic region of the polarization plots gradually increases with the Co content up to 10 wt %. Further addition of Co to 30 wt % results in no statistically significant changes to the kinetic activity but provides additional improvement in the mass transfer region of the polarization plot. The changes in activity can be well-correlated with the catalyst morphology and doped nitrogen functionalities that are dependent on the Co content during synthesis. Thus, the role of the Co species in the catalysts studied in this work appears to be simultaneously associated with the chemical (nitrogen-doped active species) and morphological (graphitized carbon nanostructures) properties of active catalytic sites (*vide supra*).

Li$-O_2$ Battery Tests. $Li-O_2$ battery tests were then carried out to further evaluate cathode catalyst performance using an electrolyte containing 1.0 mol L^{-1} $LiPF_6$ in tetraethylene glycol dimethyl ether (TEGDME) (Figure 10). These tests show a similar trend as that observed in the RDE measurements. The Co-based catalysts exhibit improved initial discharge performance relative to the control samples. In particular, the average voltage plateau of the Co-N-MWNT catalyst during discharge is ~2.85 V, significantly larger than those measured with the KJ−carbon black (~2.51 V), the metal-free N−C material (~2.62 V), and the Pt/C catalyst (~2.71 V), indicating greatly reduced ORR overpotential with much increased energy density (Figure 10a). It is worth noting that the electrical conductivity for these electrodes was measured using a four-point probe method,[47] and all of the electrodes show a comparable conductivity of around $(0.9 \pm 0.1) \times 10^4$ S m^{-1}. Thus, the observed improvement in discharge voltage in the Co-N-MWNT catalysts is not simply the result of differences in electrode conductivity. The Co-N-MWNT catalysts also deliver the highest initial discharge capacity (~3700 $mAhg_{cat}^{-1}$) among the catalysts studied including the control catalysts and Co−N−KJ (~2900 $mAhg_{cat}^{-1}$). The increased capacity is likely attributable to the increased activity associated with catalytic sites embedded on both sides of the extended graphene sheets. Additionally, the rate performance of the best performing Co-N-MWNT cathodes was further investigated at various discharging current densities (Figure 10b). A specific discharge capacity of ~3700 $mAhg_{cat}^{-1}$ obtained at a low current density of 50 mAg_{cat}^{-1} still remains as high as ~1200 $mAhg_{cat}^{-1}$ at a very high discharge current density of 800 mAg_{cat}^{-1}. This indicates good rate capacity of the cathode catalysts. Discharge−charge cycling tests up to 50 cycles were carried out with voltage cutoff of 2.5 V (discharge) and 4.1 V (charge) at a relatively high current density of 400 mAg_{cat}^{-1} (Figure 10c). The cell showed very good cycling stability up to 20 cycles without significant capacity loss; further cycling to 30 and 50 cycles results capacity losses of 8.4 and 20.4%, respectively. The discharge and charge voltage profiles of the cell at 1st and 50th cycles are compared in Figure 10d. A trace of Li_2O remains in the charged products based on XRD and Raman analyses (see below), thus, the accumulated insoluble solid particles may block the catalyst sites and O_2 transfer channels in the electrodes, thereby leading to the observed degradation. In addition, the gradual

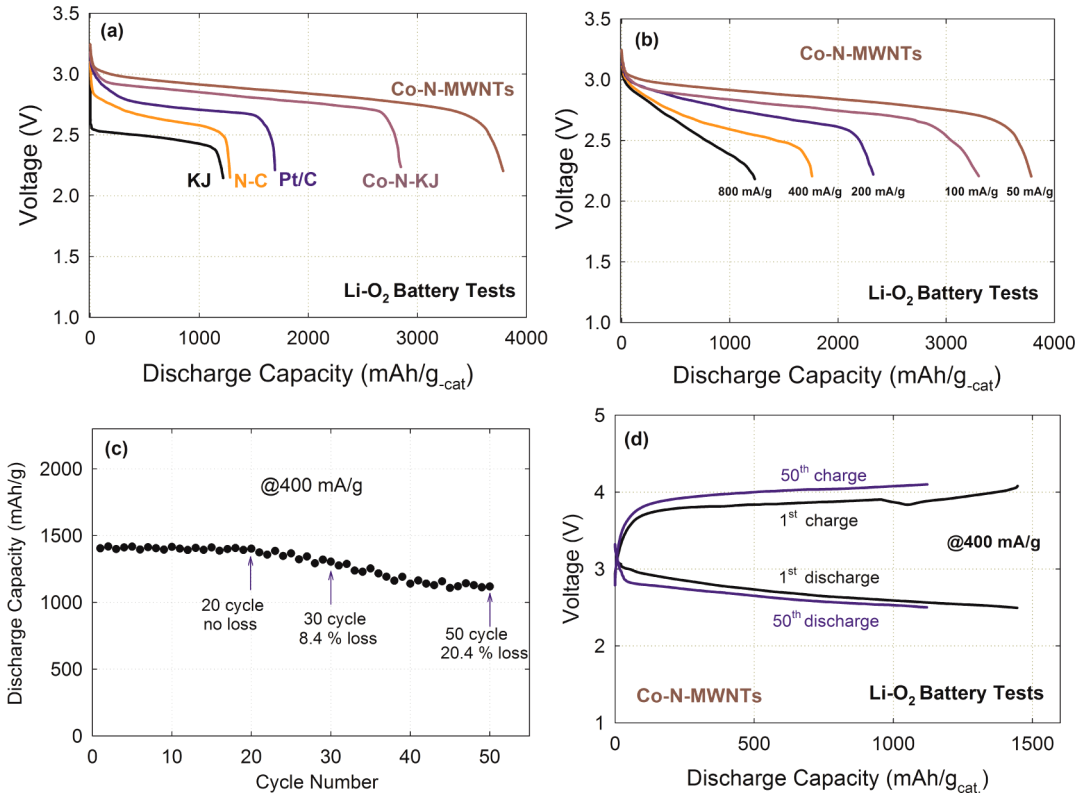

Figure 10. Li−O_2 battery tests in a dry O_2-filled glovebox at 25 °C using an electrolyte containing 1.0 mol L^{-1} $LiPF_6$ in TEGDME: (a) initial discharge performance for various catalysts at a current density of 50 mAg_{cat}^{-1}, (b) initial discharge performance for Co-N-MWNT composite catalysts at various current density from 50 to 800 mAg_{cat}^{-1}, (c) discharge−charge cycle durability tests up to 50 cycles at a current density of 400 mAg_{cat}^{-1} with voltage cutoff at 2.5 V (discharge) and 4.1 V (charge), and (d) discharge and charge voltage profiles of the cell during 1st and 50th cycles at a current density of 400 mAg_{cat}^{-1}.

loss of electrolyte due to possible evaporation is a likely reason for the observed cathode performance degradation. The cyclic durability of Li−O_2 batteries is one of the grand technical obstacles to commercialization of the advanced battery technology.[8] These results hold great promise for further development of the rechargeable Li−O_2 battery cathode using advanced electrolytes such as oligoether-functionalized silanes[48] for improved long-term cycle stability.

The products after discharging and subsequent charging process were analyzed using XRD and Raman (Figure 11). According to the XRD patterns, in addition to the Co_9S_8 phase originally belonging to the Co-N-MWNTs catalyst itself, Li_2O_2 crystalline phases were clearly observed in the discharge cathode, although a small fraction of Li_2O phase may exist. After fully charging the cathode to 4.1 V, the Li_2O_2 species formed during the discharge process were nearly eliminated. In the meantime, Raman spectra for the same cathodes studied in XRD indicate that the peaks at 790 and 250 cm^{-1} observed in the discharged cathode can be assigned to Li_2O_2, attesting that the major discharge product in the cathode is Li_2O_2. The peak around 480 and 690 cm^{-1} maybe belongs to the Co_9S_8 species in the catalysts based on a comparison to the spectrum

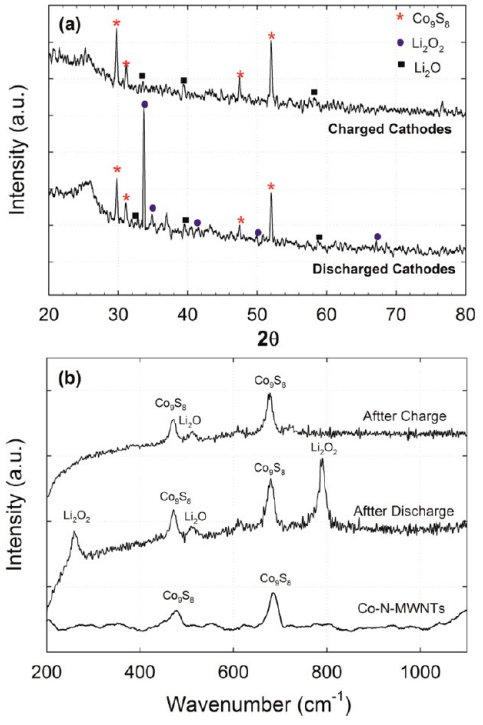

Figure 11. (a) XRD patterns and (b) Raman spectra for discharged and subsequent charged cathodes in Li−O_2 batteries using an electrolyte containing 1.0 mol L^{-1} $LiPF_6$ in TEGDME.

of a Co_9S_8-containing catalyst. The Raman analysis also suggests that the studied catalysts are able to catalyze the decomposition of Li_2O_2 during the charging process, due to the absence of Li_2O_2 in the charged cathode. Thus, the formation of Li_2O_2 appears to be reversible and is the dominant discharge product for the graphene-rich composite cathode in Li−O_2 batteries when the TEGDME-based electrolyte is used.

CONCLUSION

In summary, this work describes a new route to *in situ* synthesize nitrogen-doped graphene-rich nanocomposites with controllable morphology and doping functionalities, relative to traditional synthetic approaches for graphene materials. In this approach, an aromatic-rich heteroatom polymer, PANI, is subject to a graphitization process with the catalysis of a cobalt species using MWNTs as a supporting template. The prepared graphene-rich catalysts exhibit superior ORR activity and better performance as cathodes in nonaqueous Li−O_2 battery systems, as compared to traditional carbon black and Pt/C catalysts. An optimal temperature for heat treatment during synthesis is critical to creating a high-surface-area catalyst with favorable nitrogen doping. The addition of the Co species is found to be indispensable during synthesis for forming graphene morphology and achieving high activity, while the resulting Co_9S_8 in the catalysts plays a negligible role in ORR. Compared to the reported metal-free graphene catalysts, a higher level of quaternary and pyridinic N was identified when the catalysts are synthesized in the presence of Co, which may be concomitant with much improved activity. Promotional roles were also found for MWNTs during the formation of the graphene composites, showing extended multilayered graphene sheet morphologies. These established synthesis−structure−activity correlations provide new insights into the further optimization of chemical and physical properties in the graphene nanocomposites for the nonaqueous Li−O_2 battery cathode catalysts.

METHODS

Catalyst Synthesis. Commercial MWNTs with a Brunauer−Emmett−Teller (BET) surface area of ~230 $m^2\ g^{-1}$ were first treated in a mixed $HNO_3 + H_2SO_4$ (1:3 by volume) solution at 80 °C for 8 h. Then 0.5 g of acid-treated MWNTs was mixed with 2.0 mL of aniline dispersed in a 400 mL 0.5 M HCl solution. $Co(NO_3)_2 \cdot 6H_2O$ as a cobalt precursor with a mass of 0−8.3 g was added into the above suspension, corresponding to nominal Co content ranging from 0 to 30 wt %, as calculated against the total amount of polyaniline, sulfur, cobalt, and carbon supports. Adding oxidant solution (5.0 g of $(NH_4)_2S_2O_8$ in 100 mL of 0.5 M HCl) dropwise results in the polymerization of the aniline to produce polyaniline. After being constantly stirring for 24 h, a rotary evaporator was used to vacuum-dry the suspension followed by ball-milling for 12 h. This mixture was then heat-treated at elevated temperatures ranging from 600 to 1000 °C in an inert gas atmosphere (N_2 or Ar) for 1 h. The heat-treated samples were then preleached in 0.5 M H_2SO_4 to remove unstable species from the catalysts. The resulting final catalyst sample was denoted as Co-N-MWNTs. Typically, the yield for the catalyst synthesis approach is around 60% for the 5 wt % Co-based catalyst. An alternative nitrogen−carbon precursor, ethylenediamine, and a traditional carbon support (Ketjenblack) were also substituted into the catalyst synthesis under identical conditions as control catalyst formulations.

Characterization. Catalyst morphology was characterized by scanning electron microscopy (SEM) on an FEI Quanta 400 ESEM. High-resolution transmission electron microscopy (HR-TEM) images were taken on an FEI Titan 80-300 S/TEM. The surface area of the carbon-based catalysts was measured by Brunauer−Emmett−Teller method on an Autosorb-IQ/MP-XR instrument using nitrogen adsorption at 77 K. The pore-size distribution was determined from the adsorption isotherm using density functional theory (DFT) with slit pore geometry (Quantachrome analysis software). The crystallinity of various samples was determined by X-ray diffraction (XRD) using a Bruker AXS D8 Avance diffractometer with Cu Kα radiation. The patterns were obtained at a scan rate of 5° min^{-1} with a step of 0.02°. X-ray photoelectron spectroscopy (XPS) was performed on an ESCA 210 and MICROLAB 310D spectrometer using a Mg Kα source. High-resolution spectra were acquired with a 20 eV pass energy. The area of analysis was 700 × 300 μm in size, and each sample was analyzed at a 90° takeoff angle with a depth of 3−4 nm. All Raman spectra were obtained using a Kaiser Holospec Raman system at 514 nm excitation focused through at 100× microscope objective for a total interrogation spot size of ~1 μm. Excitation power was held constant at ~150 μW for all samples. Four individual 30 s spectra were summed for a total integration time of 120 s.

Electrochemical and Battery Measurements. RDE tests were performed using a CHI Electrochemical Station (model 750b) in a conventional three-electrode cell at a rotating disk speed of 900 rpm and room temperature. The catalyst loading on RDE was controlled at 0.6 mg cm^{-2}. A graphite rod and Ag/AgCl (3 M NaCl, 2.9 V *vs* Li/Li^+) were used as the counter and reference electrodes, respectively. ORR steady-state polarization curves were recorded in oxygen-saturated 0.1 M $LiPF_6$ in 1,2-dimethoxyethane electrolyte (DME) with a potential step of 0.03 V and a period of 30 s. Battery tests were performed on an Arbin BT-2000 battery station. The cathode catalysts were first mixed with PVDF in a mass ratio of 10:1 and dispersed in NMP by bath sonication to prepare "ink". The obtained ink was then applied to the gas diffusion layer (GDL, ELAT LT 1400W, E-TEK) by successive brush-painting until the cathode catalyst loading reached 2 mg cm^{-2}, followed by a dry in a vacuum oven at 140 °C for overnight. Then the fabricated cathode electrodes were assembled with Li metal anode and two-layer Celgard C480 separators into standard 2032 type coin cell cases (Figure S13). Optimal pattern for hole distribution and size (16 × 1.0 mm) was designed and cut by laser on the positive case for oxygen intake (Figure S13). $LiPF_6$ (1.0 mol L^{-1}) in tetraethylene glycol dimethyl ether (TEGDME) was used as electrolyte.[49,50] Discharge and charge current densities varied from 50 to 800 mA_{cat}^{-1} to study rate performance of the cathode catalysts. All battery tests were carried out at 25 °C and in a moisture-free glovebox fed by continuous O_2 flow.

Conflict of Interest: The authors declare no competing financial interest.

Acknowledgment. We gratefully acknowledge the support of the Los Alamos National Laboratory Early Career Laboratory-Directed Research and Development (LDRD) Program (20110483ER) for this work.

Supporting Information Available: Non-essential materials characterization is included in the Supporting Information. This material is available free of charge *via* the Internet at http://pubs.acs.org.

REFERENCES AND NOTES

1. Su, D. S.; Sun, G. Nonprecious-Metal Catalysts for Low-Cost Fuel Cells. *Angew. Chem., Int. Ed.* **2011**, *50*, 11570–11572.
2. Wu, G.; More, K. L.; Johnston, C. M.; Zelenay, P. High-Performance Electrocatalysts for Oxygen Reduction Derived from Polyaniline, Iron, and Cobalt. *Science* **2011**, *332*, 443–447.
3. Gong, K.; Du, F.; Xia, Z.; Durstock, M.; Dai, L. Nitrogen-Doped Carbon Nanotube Arrays with High Electrocatalytic Activity for Oxygen Reduction. *Science* **2009**, *323*, 760–764.
4. Lefevre, M.; Proietti, E.; Jaouen, F.; Dodelet, J. P. Iron-Based Catalysts with Improved Oxygen Reduction Activity in Polymer Electrolyte Fuel Cells. *Science* **2009**, *324*, 71–74.
5. Suntivich, J.; Gasteiger, H. A.; Yabuuchi, N.; Nakanishi, H.; Goodenough, J. B.; Shao-Horn, Y. Design Principles for Oxygen-Reduction Activity on Perovskite Oxide Catalysts for Fuel Cells and Metal–Air Batteries. *Nat. Chem.* **2011**, *3*, 546–550.
6. Abraham, K. M.; Jiang, Z. A Polymer Electrolyte-Based Rechargeable Lithium/Oxygen Battery. *J. Electrochem. Soc.* **1996**, *143*, 1–5.
7. Van Mierlo, J.; Maggetto, G. Fuel Cell or Battery: Electric Cars Are the Future. *Fuel Cells* **2007**, *7*, 165–173.
8. Girishkumar, G.; McCloskey, B.; Luntz, A. C.; Swanson, S.; Wilcke, W. Lithium–Air Battery: Promise and Challenges. *J. Phys. Chem. Lett.* **2010**, *1*, 2193–2203.
9. Zhang, T.; Imanishi, N.; Shimonishi, Y.; Hirano, A.; Takeda, Y.; Yamamoto, O.; Sammes, N.; Novel High, A Energy Density Rechargeable Lithium/Air Battery. *Chem. Commun.* **2010**, *46*, 1661–1663.
10. Kraytsberg, A.; Ein-Eli, Y. Review on Li-Air Batteries—Opportunities, Limitations and Perspective. *J. Power Sources* **2011**, *196*, 886–893.
11. Bruce, P. G.; Hardwick, L. J.; Abraham, K. M. Lithium–Air and Lithium–Sulfur Batteries. *MRS Bull.* **2011**, *36*, 506–512.
12. Mitchell, R. R.; Gallant, B. M.; Thompson, C. V.; Shao-Horn, Y. All-Carbon-Nanofiber Electrodes for High-Energy Rechargeable Li-O_2 Batteries. *Energy Environ. Sci.* **2011**, *4*, 2952–2958.
13. Ogasawara, T.; Debart, A.; Holzapfel, M.; Novak, P.; Bruce, P. G. Rechargeable Li_2O_2 Electrode for Lithium Batteries. *J. Am. Chem. Soc.* **2006**, *128*, 1390–1393.
14. Debart, A.; Paterson, A. J.; Bao, J.; Bruce, P. G. α-MnO_2 Nanowires: A Catalyst for the O_2 Electrode in Rechargeable Lithium Batteries. *Angew. Chem., Int. Ed.* **2008**, *47*, 4521–4524.
15. Zhang, S. S.; Ren, X. M.; Read, J. Heat-Treated Metal Phthalocyanine Complex as an Oxygen Reduction Catalyst for Non-aqueous Electrolyte Li/Air Batteries. *Electrochim. Acta* **2011**, *56*, 4544–4548.
16. Lu, Y. C.; Xu, Z. C.; Gasteiger, H. A.; Chen, S.; Hamad-Schifferli, K.; Shao-Horn, Y. Platinum–Gold Nanoparticles: A Highly Active Bifunctional Electrocatalyst for Rechargeable Lithium–Air Batteries. *J. Am. Chem. Soc.* **2010**, *132*, 12170–12171.
17. Wang, H.; Yang, Y.; Liang, Y.; Zheng, G.; Li, Y.; Cui, Y.; Dai, H. Rechargeable Li–O_2 Batteries with a Covalently Coupled $MnCo_2O_4$–Graphene Hybrid as an Oxygen Cathode Catalyst. *Energy Environ. Sci.* **2012**, *5*, 7931–7935.
18. Laoire, C. O.; Mukerjee, S.; Abraham, K. M.; Plichta, E. J.; Hendrickson, M. A. Elucidating the Mechanism of Oxygen Reduction for Lithium–Air Battery Applications. *J. Phys. Chem. C* **2009**, *113*, 20127–20134.
19. Shao, Y.; Park, S.; Xiao, J.; Zhang, J.-G.; Wang, Y.; Liu, J. Electrocatalysts for Nonaqueous Lithium–Air Batteries: Status, Challenges, and Perspective. *ACS Catal.* **2012**, *2*, 844–857.
20. Liang, Y. Y.; Li, Y. G.; Wang, H. L.; Zhou, J. G.; Wang, J.; Regier, T.; Dai, H. J. Co_3O_4 Nanocrystals on Graphene as a Synergistic Catalyst for Oxygen Reduction Reaction. *Nat. Mater.* **2011**, *10*, 780–786.
21. Byon, H. R.; Suntivich, J.; Shao-Horn, Y. Graphene-Based Non-Noble-Metal Catalysts for Oxygen Reduction Reaction in Acid. *Chem. Mater.* **2011**, *23*, 3421–3428.
22. Wang, S. Y.; Yu, D. S.; Dai, L. M.; Chang, D. W.; Baek, J. B. Polyelectrolyte-Functionalized Graphene as Metal-Free Electrocatalysts for Oxygen Reduction. *ACS Nano* **2011**, *5*, 6202–6209.
23. Wang, L.; Zhao, X.; Lu, Y.; Xu, M.; Zhang, D.; Ruoff, R. S.; Stevenson, K. J.; Goodenough, J. B. $CoMn_2O_4$ Spinel Nanoparticles Grown on Graphene as Bifunctional Catalyst for Lithium–Air Batteries. *J. Electrochem. Soc.* **2011**, *158*, A1379–A1382.
24. Choi, J.-Y.; Higgins, D.; Chen, Z. Highly Durable Graphene Nanosheet Supported Iron Catalyst for Oxygen Reduction Reaction in PEM Fuel Cells. *J. Electrochem. Soc.* **2012**, *159*, B87–B90.
25. Lai, L.; Potts, J. R.; Zhan, D.; Wang, L.; Poh, C. K.; Tang, C.; Gong, H.; Shen, Z.; Lin, J.; Ruoff, R. S. Exploration of the Active Center Structure of Nitrogen-Doped Graphene-Based Catalysts for Oxygen Reduction Reaction. *Energy Environ. Sci.* **2012**, *5*, 7936–7942.
26. Li, Y.; Wang, J.; Li, X.; Geng, D.; Banis, M. N.; Li, R.; Sun, X. Nitrogen-Doped Graphene Nanosheets as Cathode Materials with Excellent Electrocatalytic Activity for High Capacity Lithium–Oxygen Batteries. *Electrochem. Commun.* **2012**, *18*, 12–15.
27. Shao, Y.; Liu, J.; Wang, Y.; Lin, Y. Novel Catalyst Support Materials for PEM Fuel Cells: Current Status and Future Prospects. *J. Mater. Chem.* **2009**, *19*, 46–59.
28. Wu, G.; Artyushkova, K.; Ferrandon, M.; Kropf, A. J.; Myers, D.; Zelenay, P. Performance Durability of Polyaniline-Derived Non-precious Cathode Catalysts. *ECS Trans.* **2009**, *25*, 1299–1311.
29. Stankovich, S.; Dikin, D. A.; Piner, R. D.; Kohlhaas, K. A.; Kleinhammes, A.; Jia, Y.; Wu, Y.; Nguyen, S. T.; Ruoff, R. S. Synthesis of Graphene-Based Nanosheets *via* Chemical Reduction of Exfoliated Graphite Oxide. *Carbon* **2007**, *45*, 1558–1565.
30. Qu, L. T.; Liu, Y.; Baek, J. B.; Dai, L. M. Nitrogen-Doped Graphene as Efficient Metal-Free Electrocatalyst for Oxygen Reduction in Fuel Cells. *ACS Nano* **2010**, *4*, 1321–1326.
31. Wu, G.; Nelson, M.; Ma, S. G.; Meng, H.; Cui, G. F.; Shen, P. K. Synthesis of Nitrogen-Doped Onion-like Carbon and Its Use in Carbon-Based CoFe Binary Non-Precious-Metal Catalysts for Oxygen-Reduction. *Carbon* **2011**, *49*, 3972–3982.
32. Wang, Z. H.; Pan, L.; Hu, H. B.; Zhao, S. P. Co_9S_8 Nanotubes Synthesized on the Basis of Nanoscale Kirkendall Effect and Their Magnetic and Electrochemical Properties. *CrystEngComm* **2010**, *12*, 1899–1904.
33. Yin, P. F.; Sun, L. L.; Gao, Y. L.; Wang, S. Y. Preparation and Characterization of Co_9S_8 Nanocrystalline and Nanorods. *Bull. Mater. Sci.* **2008**, *31*, 593–596.
34. Gao, W.; Singh, N.; Song, L.; Liu, Z.; Reddy, A. L. M.; Ci, L.; Vajtai, R.; Zhang, Q.; Wei, B.; Ajayan, P. M. Direct Laser Writing of Micro-Supercapacitors on Hydrated Graphite Oxide Films. *Nat. Nanotechnol.* **2011**, *6*, 496–500.
35. Pels, J. R.; Kapteijn, F.; Moulijn, J. A.; Zhu, Q.; Thomas, K. M. Evolution of Nitrogen Functionalities in Carbonaceous Materials during Pyrolysis. *Carbon* **1995**, *33*, 1641–1653.
36. Qie, L.; Chen, W.-M.; Wang, Z.-H.; Shao, Q.-G.; Li, X.; Yuan, L.-X.; Hu, X.-L.; Zhang, W.-X.; Huang, Y.-H. Nitrogen-Doped Porous Carbon Nanofiber Webs as Anodes for Lithium Ion Batteries with a Superhigh Capacity and Rate Capability. *Adv. Mater.* **2012**, *24*, 2047–2050.
37. Wu, G.; Nelson, M. A.; Mack, N. H.; Ma, S. G.; Sekhar, P.; Garzon, F. H.; Zelenay, P. Titanium Dioxide-Supported Non-precious Metal Oxygen Reduction Electrocatalyst. *Chem. Commun.* **2010**, *46*, 7489–7491.
38. Matter, P. H.; Zhang, L.; Ozkan, U. S. The Role of Nanostructure in Nitrogen-Containing Carbon Catalysts for the Oxygen Reduction Reaction. *J. Catal.* **2006**, *239*, 83–96.
39. Wu, G.; Li, L.; Li, J.-H.; Xu, B.-Q. Polyaniline-Carbon Composite Films as Supports of Pt and PtRu Particles for Methanol Electrooxidation. *Carbon* **2005**, *43*, 2579–2587.
40. Wu, G.; Johnston, C. M.; Mack, N. H.; Artyushkova, K.; Ferrandon, M.; Nelson, M.; Lezama-Pacheco, J. S.; Conradson,

S. D.; More, K. L.; Myers, D. J.; *et al.* Synthesis-Structure-Performance Correlation for Polyaniline-Me-C Non-precious Metal Cathode Catalysts for Oxygen Reduction in Fuel Cells. *J. Mater. Chem.* **2011**, *21*, 11392–11405.
41. Holby, E. F.; Taylor, C. D. Control of Graphene Nanoribbon Vacancies by Fe and N Dopants: Implications for Catalysis. *Appl. Phys. Lett.* **2012**, *101*, 064102.
42. Tuinstra, F.; Koenig, J. L. Raman Spectrum of Graphite. *J. Chem. Phys.* **1970**, *53*, 1126–1130.
43. Herrmann, I.; Kramm, U. I.; Radnik, J.; Fiechter, S.; Bogdanoff, P. Influence of Sulfur on the Pyrolysis of Cotmpp as Electrocatalyst for the Oxygen Reduction Reaction. *J. Electrochem. Soc.* **2009**, *156*, B1283–B1292.
44. Laoire, C. O.; Mukerjee, S.; Abraham, K. M.; Plichta, E. J.; Hendrickson, M. A. Influence of Nonaqueous Solvents on the Electrochemistry of Oxygen in the Rechargeable Lithium−Air Battery. *J. Phys. Chem. C* **2010**, *114*, 9178–9186.
45. Zhu, Y.; Murali, S.; Stoller, M. D.; Ganesh, K. J.; Cai, W.; Ferreira, P. J.; Pirkle, A.; Wallace, R. M.; Cychosz, K. A.; Thommes, M.; *et al.* Carbon-Based Supercapacitors Produced by Activation of Graphene. *Science* **2011**, *332*, 1537–1541.
46. Easton, E. B.; Yang, R.; Bonakdarpour, A.; Dahn, J. R. Thermal Evolution of the Structure and Activity of Magnetron-Sputtered TM-C-N (TM = Fe, Co) Oxygen Reduction Catalysts. *Electrochem. Solid-State Lett.* **2007**, *10*, B6–B10.
47. Gao, W.; Alemany, L. B.; Ci, L.; Ajayan, P. M. New Insights into the Structure and Reduction of Graphite Oxide. *Nat. Chem.* **2009**, *1*, 403–408.
48. Zhang, Z.; Lu, J.; Assary, R. S.; Du, P.; Wang, H.-H.; Sun, Y.-K.; Qin, Y.; Lau, K. C.; Greeley, J.; Redfern, P. C.; *et al.* Increased Stability toward Oxygen Reduction Products for Lithium−Air Batteries with Oligoether-Functionalized Silane Electrolytes. *J. Phys. Chem. C* **2011**, *115*, 25535–25542.
49. Jung, H.-G.; Hassoun, J.; Park, J.-B.; Sun, Y.-K.; Scrosati, B. An Improved High-Performance Lithium−Air Battery. *Nat. Chem.* **2012**, *4*, 579–585.
50. Laoire, C.; Mukerjee, S.; Plichta, E. J.; Hendrickson, M. A.; Abraham, K. M. Rechargeable Lithium/TEGDME-$LiPF_6$/O_2 Battery. *J. Electrochem. Soc.* **2011**, *158*, A302–A308.